

pubs.acs.org/JPCA Article

Photophysical Outcomes of Water-Solvated Heterocycles: Single-Conformation Ultraviolet and Infrared Spectroscopy of Microsolvated 2-Phenylpyrrole

Published as part of The Journal of Physical Chemistry A virtual special issue "Marsha I. Lester Festschrift". Ruby W. Neisser, John P. Davis, Megan E. Alfieri, Hayden Harkins, Andrew S. Petit,* Daniel P. Tabor,* and Nathanael M. Kidwell*



Cite This: J. Phys. Chem. A 2023, 127, 10540-10554



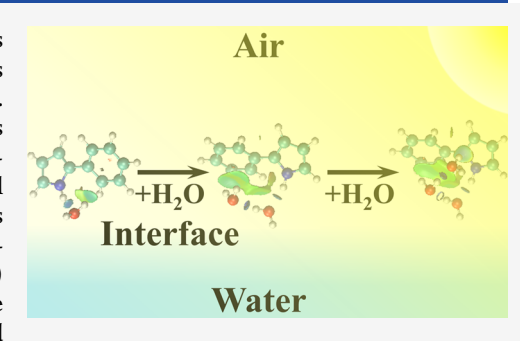
ACCESS

III Metrics & More

Article Recommendations

s) Supporting Information

ABSTRACT: The molecular chromophores within brown carbon (BrC) aerosols absorb solar radiation at visible and near-ultraviolet wavelengths. This contributes to the overall warming of the troposphere and the photochemical aging of aerosols. In this investigation, we combine a suite of experimental and theoretical methods to reveal the conformation-specific ultraviolet and infrared spectroscopy of 2-phenylpyrrole (2PhPy)—an extended π -conjugated pyrrole derivative and a model BrC chromophore—along with its water microsolvated molecular complexes (2PhPy:nH₂O, n = 1–3). Using resonant two-photon ionization and double-resonance holeburning techniques alongside MP3 (ground state) and ADC(3) (excited state) torsional potential energy surfaces and discrete variable representation simulations, we characterized the ultraviolet spectra of 2PhPy and



2PhPy:1H₂O. This analysis revealed evidence for Herzberg–Teller vibronic coupling along the CH wagging and NH stretching coordinates of the aromatic rings. Conformation-specific infrared spectroscopy revealed extended hydrogen-bonding networks of the 2PhPy:nH₂O complexes. Upon stepwise addition of H₂O solvation, the nearest H₂O acceptor forms a strong, noncovalent interaction with the pyrrole NH donor, while the second and third H₂O partners interface with the phenyl and pyrrole aromatic rings through growing van der Waals π /H atom stabilization. A local-mode Hamiltonian approach was employed for comparison with the experimental spectra, thus identifying the vibrational spectral signatures to specific 2PhPy:nH₂O oscillators.

■ INTRODUCTION

Atmospheric aerosols are known to exert a profound influence on the Earth's radiative balance, directly impacting climate and air quality. Brown carbon (BrC), a component of aerosols originating from both natural and anthropogenic sources, has recently gained significant attention due to its light-absorbing properties. The absorption of solar radiation by BrC aerosols can lead to localized warming, altering atmospheric chemistry and regional climate patterns. Understanding the underlying mechanisms of BrC aerosol absorption is crucial for accurate climate modeling and air quality predictions.

Nitrogen-containing heterocycles (N-heterocycles) have emerged as prominent molecular chromophores generated within the BrC aerosol environment. The formation mechanism of N-heterocycles is believed to be first initiated by the production of isoprene oxidation products. Galloway reported that the oxidation of ambient isoprene by OH radicals under NO_x conditions creates small water-soluble carbonyl compounds such as glyoxal, methylglyoxal, glycolaldehyde, and hydroxyacetone. Subsequently, isoprene oxidation products may partition into aqueous aerosols and may undergo a Maillard-type browning reaction with ammonium salts and

amines to form *N*-heterocycles.⁵ Derivatives of imidazoles and pyrroles are among the candidate *N*-heterocycle chromophores plausibly formed in BrC aerosols, whose solar absorption coefficients are wavelength dependent. In particular, 2-phenylpyrrole (2PhPy) in Figure 1 is a model BrC chromophore, and its absorption extends into the visible and near-UV regions. However, the photophysical processes responsible for the absorption characteristics of 2PhPy and the local solvation environment's role in altering the accessible absorption pathways are not yet fully understood.

The intermolecular interactions between solvent molecules, such as water, and molecular chromophores have dramatic implications on the conformational isomer shapes. As a result, these noncovalent interactions steer the photophysical and

Received: July 3, 2023

Revised: November 15, 2023 Accepted: November 17, 2023 Published: December 12, 2023





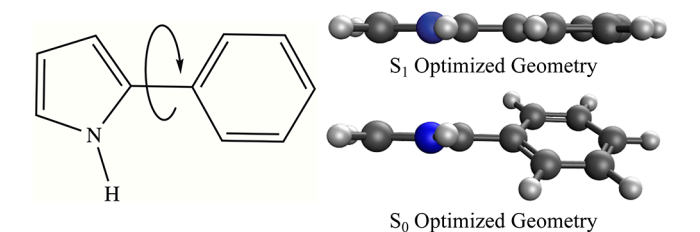


Figure 1. Molecular structure of 2-phenylpyrrole with the NC–CC torsional motion highlighted. The S_{0^-} and S_1 -optimized geometries shown at the right differ significantly along the NC–CC torsional coordinate, suggesting that this vibrational mode will have a pronounced Franck–Condon progression in the $S_1 \leftarrow S_0$ vibronic spectroscopy.

photochemical outcomes in condensed-phase environments. Recent studies have indicated that the molecular photodynamics at air/water interfaces can be dramatically different than the absorption outcomes in the bulk phase. 7-10 Chemical pathways that would otherwise be thermodynamically or kinetically unfavorable in the bulk, aqueous phase may be possible or even accelerated at the aerosol interface. Partial solvation at the air/water interface intrinsically creates a unique, asymmetric environment, whereby molecular chromophores may adopt atypical hydrogen-bonding networks with nearby water solvent, leading to altered entropic barriers.¹¹ Revealing the interfacial morphology of BrC chromophores, such as 2PhPy, is thus important for understanding the photochemical processing and aging of BrC aerosols. Indeed, microsolvated solute:nH2O complexes mimic the partially solvated configurations at air/water aerosol interfaces. Therefore, investigating the stepwise addition of water solvation surrounding BrC chromophores with conformation specificity is important to developing a molecular-level framework of solar absorption mechanisms at aerosol interfaces.

Upon electronic absorption, 2PhPy may undergo a $S_2 \leftarrow S_0$ transition with $\pi^* \leftarrow \pi$ electronic character. Alternatively, a S_1 \leftarrow S₀ excitation may be accessed that can be described as a linear combination of a locally excited (LE) $\pi^* \leftarrow \pi$ transition centered on the phenyl ring and a twisted intramolecular charge transfer (TICT) transition. The TICT transition is characteristic of electron charge migration from the pyrrole ring donor to the phenyl ring acceptor. The extent to which intramolecular charge will transfer between aromatic ring systems is determined by the NC-CC dihedral angle of 2PhPy highlighted in Figure 1, and this charge transfer may be mediated by the chromophore's hydrogen-bonding configuration with water. Furthermore, intramolecular charge transfer may compete with intermolecular charge transfer from the pyrrole π -system to the surrounding water solvation environment. Sobolewski and Domcke¹² determined that photoejection of electron charge from pyrrole chromophores to the aqueous environment is possible from their studies on pyrrole:nH2O complexes. Such a photosensitization pathway is hallmarked by the generation of the hydrated electron at the air/water interface 7,13,14 and may be a mechanism to radicalinitiated reactions and enriched chemical complexity in aerosols.

In this work, we build on our previous study on 1-phenylpyrrole, ¹⁵ and we focus on the spectroscopic properties of the 2PhPy:nH₂O molecular complexes and the role of intermolecular interactions in shaping the conformational

isomer orientations and the photophysical mechanisms. To investigate these phenomena, we employ an array of singleconformation infrared (IR) and ultraviolet (UV) laser spectroscopy techniques to probe the structure and excited state dynamics of the 2PhPy:nH2O complexes. In addition to leveraging electronic structure methods to elucidate the electronic character of the excited states of 2PhPy and 2PhPy:1H₂O, we model the UV spectroscopy results using discrete variable representation (DVR) calculations on fitted torsional potential energy surfaces. Furthermore, we interpret the ground state IR spectra using local mode Hamiltonian simulations. By combining experimental and theoretical approaches, we aim to unravel the details of charge transfer and the dependence on water solvation to shed light on the optical properties of BrC chromophores at the aerosol air/ water interface.

EXPERIMENTAL METHODS

All experiments were performed in a custom, high-vacuum mass spectrometer with imaging capabilities described previously. 15,16 2-Phenylpyrrole (2PhPy) was purchased from Sigma-Aldrich (99%) and used without further purification. To obtain sufficient vapor pressure, 2PhPy was stored and heated to 135 °C in a stainless-steel sample compartment behind a 500 μ m pulse valve nozzle (Parker General Valve, Series 9). Furthermore, another sample reservoir attached to the same gas line as 2PhPy contained a small amount of water that was gently heated to 30 °C. During experiments, the vapor of 2PhPy and a small percentage of water (<0.5%) were entrained in $\sim 3-3.5$ bar of helium and subsequently pulsed into the high-vacuum chamber at 10 Hz. Therefore, a supersonic jet expansion was formed, where adiabatic collisions of the inert carrier gas with 2PhPy and molecular complexes with water (2PhPy:nH₂O; n = 1-3) were cooled to their respective zeropoint energy levels. Subsequently, selection of the coldest molecular complexes was performed using a skimmer (2 mm ID, Beam Dynamics) positioned 30 mm downstream, after which an array of laser-based spectroscopy methods was employed in the collision-free region of the molecular beam.

Tunable UV radiation was generated by doubling the output frequency from a Nd:YAG pumped dye laser (Radiant Dyes NarrowScan) using an Inrad Autotracker III equipped with a β -barium borate (BBO) crystal. To obtain vibrationally resolved spectra in the excited electronic state in a massresolved fashion, resonant two-photon ionization (R2PI) spectroscopy was performed for $2PhPy:nH_2O$ (n = 0-3). Excitation of 2PhPy: nH_2O (n = 0-3) to vibronic levels was performed with the UV probe laser, and another UV photon from this same radiation source was also used to ionize the excited state population. The target mass ion signal was gated and monitored as a function of the UV probe laser wavelength to collect the R2PI spectra. While obtaining the R2PI spectra, we ensured that the transition intensities were not saturated using ~0.2 mJ/pulse UV power. Therefore, the intensities represent the true absorption intensities of each transition band.

To determine if multiple conformational isomers were present for $2\text{PhPy:}n\text{H}_2\text{O}$ (n=0-3), several double-resonance methods were utilized. Ultraviolet holeburning (UV HB) spectroscopy was conducted by fixing a UV holeburn laser wavelength from another Nd:YAG-pumped dye laser (Continuum Surelite II-10, Radiant Dyes NarrowScan K; 5 Hz) on a vibronic transition belonging to a unique conformational

isomer. Then, the counterpropagating and spatially overlapped UV probe laser from the R2PI method scanned the wavelength region of interest. With the UV holeburn laser preceding the UV probe laser by approximately 50 ns, a sizable fraction of the ground state conformational isomer population was removed. As the UV probe laser was scanned and became resonant with a transition that shared a common zero-point energy level with the UV holeburn laser, a depletion in the probed mass ion signal was recorded as a function of the UV probe wavelength. Therefore, a difference spectrum was obtained by monitoring the gated mass ion probe signal using active baseline subtraction and averaging the signal depletion with respect to the wavelength of the UV probe laser. Therefore, the number of possible 2PhPy:nH2O conformational isomers could be identified by observing all or a partial number of vibronic transitions appearing in the UV HB spectrum compared to the R2PI spectrum. In so doing, conformationspecific UV spectra were obtained for the 2PhPy:nH2O complex isomers.

In a similar manner, infrared holeburning (IR HB) spectroscopy was performed by using a unique IR transition belonging to a 2PhPy:nH2O conformational isomer as the holeburn source and averaging the scanned UV probe mass ion signal as a function of the UV wavelength. Furthermore, to obtain single-conformation IR spectra used for the IR HB experiments, resonant ion-depletion infrared (RIDIR) spectroscopy was employed. Here, the IR laser scanned from 2900 to 4000 cm⁻¹ while the UV probe laser was fixed on a vibronic transition for a distinct 2PhPy:nH₂O isomer. Whenever the IR laser shared a common ground state zero-point energy level as the conformational isomer monitored with the UV probe laser, a depletion was observed in the mass ion signal, which was collected as a function of the IR wavelength. Nonresonant iondepletion infrared (nRIDIR) spectroscopy uses the same temporal and spatial alignment of the lasers used for the RIDIR method, but the UV probe laser wavelength is not fixed on a resonant transition. In this case, the IR spectrum is not conformation specific. During experiments, the conditions were optimized to minimize complex ion fragmentation from higher-order complexes when a small percentage of water was used in the gas flow. The experimental conditions were regularly adjusted in real time to increase the ion signal in the mass channel of interest while decreasing the ion signal of larger complexes. The photoionization cross sections may be different, however, for larger complexes, so complex ion fragmentation cannot be entirely ruled out.

Fluorescence emission and absorption studies for solutionphase samples of dissolved 2PhPy were performed using an Agilent Cary Eclipse fluorescence spectrophotometer (G9800A). Here, ~0.0043 g of 2PhPy was dissolved in a series of standard solutions with increasing solvent polarity and % volume ratios composed of tetrahydrofuran (Fischer-Scientific, 100%) and ultrapure water, THF:H₂O. Namely, 20 mL glass vials of 100:0, 80:20, 60:40, and 20:80% volume ratios of THF:H2O were prepared, from which 1 mL of each sample solution was placed in a 1 cm quartz cuvette for the solution-phase spectroscopy experiments. Absorption measurements were collected from 190 to 345 nm, using an emission wavelength of 350 nm. Furthermore, fluorescence emission experiments were performed from 320 to 800 nm with an excitation wavelength of 315 nm. These studies were conducted using the following experimental parameters: 480 V photomultiplier tube voltage, 5 nm slit width, and 1 nm scan

resolution. Averages consisting of three independent scans were recorded for each % volume THF:H₂O sample.

COMPUTATIONAL METHODS

A configurational search approach was performed to identify the ground state minimum-energy geometries of 2PhPy:nH₂O (n = 0-3). First, the ABCluster program¹⁷ was used to determine initial conformational isomer structures. Here, the artificial bee colony (ABC) algorithm generated local and global minima of 2PhPy: nH_2O (n = 0-3) geometries within an 80 kJ/mol energy window of the lowest-energy isomer. Next, the lowest-energy conformational isomers were identified by using quantum chemical calculations within the Gaussian16 Ground state geometry optimization and vibrational frequency calculations were performed at the density functional theory (DFT) ω B97X-D/6-311++G(d,p) level, and true minima were verified by ensuring that all vibrational frequencies were real. Previously used to model charge transfer more effectively than other functionals, ¹⁹ the ω B97X-D functional was chosen to describe the intermolecular interactions between 2PhPy and nH2O molecules.

The vertical excitation energies of 2PhPy and 2PhPy:1H₂O were calculated by using a variety of electronic structure methods at the S₀-optimized geometry. The simplest approach utilized TD-ωB97X-D/def2-TZVPPD//ωB97X-D/def2-SVPD. We additionally calculated the vertical excitation energies using ADC(2), ADC(3), and EOM-EE-CCSD at geometries optimized using CCSD/aug-cc-pVDZ for 2PhPy and CCSD/jul-cc-pVDZ for 2PhPy:1H2O. The resolution of identity approximation was used in the ADC(2) and ADC(3) calculations. The methods ADC(2) and EOM-EE-CCSD are known to generally provide a more accurate description of electronic excitation energies than TD-DFT. 20,21 As a thirdorder method, ADC(3) often provides an improved description of electronic excited states, particularly those with significant double excitation character. ^{22,23} In addition to the electronic excitation energies, we analyzed the electronic character of the states using natural transition orbitals (NTOs).^{24,25} All of these electronic structure calculations were performed using Q-Chem 6.026 and analyzed using IQmol 3.0.1.

We performed relaxed scans along the NC–CC dihedral angle, ϕ_{scan} , on both S_0 and S_1 . We used CCSD to perform the scans on S_0 and EOM-EE-CCSD to perform the scans on S_1 with an aug-cc-pVDZ basis for 2PhPy and a jul-cc-pVDZ basis for 2PhPy:1H₂O. Single-point energies at the optimized geometries were evaluated by using MP3 on S_0 and ADC(3) on S_1 ; the same basis sets were employed for these as for the geometry optimizations. We used MP3 for the ground state single-point energies to be consistent with how the excited-state single-point energies are described. Exploratory relaxed scans for other degrees of freedom (NH stretch, NH wag, and CH wags) were also performed on S_0 by using the same level of theory.

■ SIMULATION METHODS

DVR Calculations for Vibronic Spectroscopy. Once the potential energy surfaces were obtained at the MP3 (ground state) and ADC(3) (excited state) levels of theory, the calculation of the vibronic spectra was performed in a manner similar to prior work on microsolvated 1-phenylpyrrole with $\rm H_2O.^{15}$ The symmetrized torsional potential energy surfaces

(the average of the four dihedral angles found in constrained optimizations about the C-N torsion, ϕ_{symm}) were fit to a cubic spline interpolation that was constrained to be periodic. This explicit fit was used as the potential surface calculating the wave functions using the discrete variable representation (DVR) method.²⁷ In the calculations in the paper, the number of grid points was set to 1001, after testing for convergence. This model has several empirical parameters, including shifting the origin of the progression and the relative intensity (and offset) of subsequent vibrational progressions. In addition, though the effective mass of the torsional coordinate can be calculated from the molecular geometry, 28 we choose to implement this as an empirical parameter, 15,29 both to compensate for any systematic errors in torsional potential frequencies and due to the potential motion of the other degrees of freedom along the torsional coordinate. We discuss these parameters below when presenting the spectral fits.

Vibrational Spectroscopy Methods. The vibrational spectra were calculated from the ωB97X-D/6-311+G(d,p) level of theory (optimization and harmonic frequency calculations with the Gaussian16 suite 18) using a reduceddimensional local mode model Hamiltonian framework.³⁰ Because the lower frequency (strongly hydrogen-bonded) OH stretches (and NH) are close in frequency to twice the bending overtone of water, the spectra can be affected by Fermi resonance interactions. The procedure for obtaining an estimated anharmonic spectrum is as follows. First, a set of local mode OH (and NH) stretch vectors are obtained by rediagonalizing the mass-weighted Cartesian force constant matrix with all other atoms (other than the XH stretch of interest) multiplied by a large number (in this case, 25). When rediagonalized, the highest frequency mode is a localized stretch on the desired XH oscillator. Then, an orthogonal transformation is found between the original normal mode coordinates and the local mode vectors. A similar procedure is employed for the HOH bending modes and the NH wagging modes. The overall Hamiltonian (and linear dipole operator) is transformed to this local mode representation at the harmonic level. Then the stretches are coupled to the bend overtones (and the NH wagging overtone) through an empirical parameter. These couplings for H₂O were previously explicitly calculated (through a reduced dimensional expansion), and the couplings are on the order of 45.0 cm⁻¹ in the local mode basis. As the NH stretching frequency is the lowest local mode frequency in each of the clusters and there are a set of 2PhPy ring modes (involving the wagging of the NH bond) around 1600 cm⁻¹, two NH wagging modes were included in the local mode Hamiltonian. The coupling between these states is approximated through both empirical fitting and comparison of the relevant force constants in a reduced dimensional normal mode anharmonic calculation.

RESULTS

Computational Results. Figure 2 summarizes the excitation energies, oscillator strengths, and electronic characters of the S_1 , S_2 , and S_3 states of 2PhPy at the ADC(3)/aug-cc-pVDZ//CCSD/aug-cc-pVDZ level of theory. The S_1 state exhibits significant multiconfigurational character, with two pairs of natural transition orbitals (NTOs) required to accurately represent the transition. The dominant NTO exhibits significant charge-transfer character with electron density transitioning from being delocalized across both rings to being localized on the phenyl ring. The other NTO is a π^*

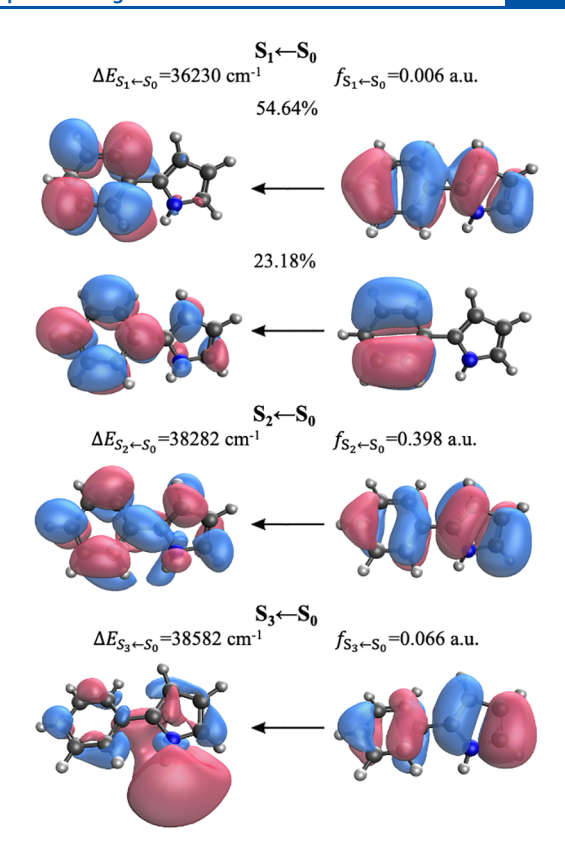


Figure 2. Natural transition orbitals (NTOs) for the $S_1 \leftarrow S_0$, $S_2 \leftarrow S_0$, and $S_3 \leftarrow S_0$ transitions of 2PhPy evaluated at the S_0 -optimized geometry. The calculations were performed at the ADC(3)/aug-cc-pVDZ//CCSD/aug-cc-pVDZ level of theory, and the orbitals are plotted with an isovalue of 0.06. The $S_1 \leftarrow S_0$ transition has significant multiconfigurational character, with the percentages denoting how much each pair of NTOs contributes to the overall transition. In contrast, the $S_2 \leftarrow S_0$ and $S_3 \leftarrow S_0$ transitions are each well-described by a single pair of NTOs.

 $\leftarrow \pi$ transition that is localized on the phenyl ring. In contrast, the S2 and S3 states are each well-described by a single NTO pair. The S_2 state has clear $\pi^* \leftarrow \pi$ character, with both NTOs being delocalized across both rings, while the S_3 state is $\sigma^* \leftarrow$ π , with electron density shifting into the region outside of the NH bond. Turning to the vertical excitation energies, the calculated $\Delta E_{S_1 \leftarrow S_0} = 36230 \text{ cm}^{-1}$ is in much better agreement with the experimentally observed transition range, 33406-34106 cm⁻¹, than the calculated $\Delta E_{S_2 \leftarrow S_0} = 38282$ cm⁻¹ or $\Delta E_{S_3 \leftarrow S_0} = 38582 \text{ cm}^{-1}$. The S₂ state is much brighter than S₁, $f_{S_2 \leftarrow S_0} = 0.398$ au compared to $f_{S_1 \leftarrow S_0} = 0.006$ au, although, importantly, our calculations suggest that the $S_1 \leftarrow S_0$ transition is not totally dark. Further differences between the transition dipole moments of the $S_1 \leftarrow S_0$ and $S_2 \leftarrow S_0$ transitions are summarized in Table S1. Specifically, the transition dipole moment for the $S_2 \leftarrow S_0$ transition is predominately aligned with the long a-axis of 2PhPy whereas the transition dipole moment for the $S_1 \leftarrow S_0$ transition has significant components along both the a- and b-axes (see Figure S1 for the definition of these axes). Finally, we note that the S₀-S₁ adiabatic energy gap, evaluated as the difference in the electronic energies of the S₀ and S₁ states at each of their optimized geometries, is 33964 cm⁻¹; this provides an estimate for the origin band of the $S_1 \leftarrow S_0$ transition. The $S_2 \leftarrow S_0$ adiabatic energy gap, at 35052 cm⁻¹, lies significantly above the experimental transition range.

Table S2 summarizes our benchmarking of the vertical excitation energies and oscillator strengths of 2PhPy. The EOM-EE-CCSD, ADC(2), and ADC(3) calculations provide a consistent picture of the S₁, S₂, and S₃ states, with S₂ being a bright $\pi^* \leftarrow \pi$ state, S_3 being a darker $\sigma^* \leftarrow \pi$ state, and S_1 being a darker $\pi^* \leftarrow \pi$ state with a more complex electronic structure and some degree of charge-transfer character. Changing the excited state methodology from ADC(2) to ADC(3) results in improved agreement between the calculated $\Delta E_{S_1 \leftarrow S_0}$ and the experimental transition range; the calculated $\Delta E_{S_1 + S_0}$ is 37658 cm⁻¹ with ADC(2) and 36230 cm⁻¹ with ADC(3). The EOM-EE-CCSD calculations overestimate the vertical excitation energy more than the ADC methods, with the EOM-EE-CCSD $\Delta E_{S_1 \leftarrow S_0} = 38085$ cm⁻¹. For all three methods, increasing the size of basis used in the single-point calculations has a modest effect on the calculated vertical excitation energies and oscillator strengths. For example, performing the ADC(3) calculation with the larger jun-ccpVTZ basis set results in $\Delta E_{S_1 \leftarrow S_0} = 36074 \text{ cm}^{-1}$ and an unchanged $f_{S_1 \leftarrow S_0} = 0.006$ au Interestingly, TD- ω B97X-D predicts an incorrect state ordering, with S1 described as the bright $\pi^* \leftarrow \pi$ state with an excitation energy of 38386 cm⁻¹. Finally, we posit that some of the computational challenges associated with accurately capturing the electronic excited states of 2PhPy originate from the presence of non-negligible doubly excited state character in S₁ and S₂. Specifically, the squared norm of the one-electron transition density matrix of the S₁ and S₂ states is 0.79 and 0.82, respectively, at the ADC(3)/aug-cc-pVDZ level of theory. This indicates that double (and higher-order) excitations account for 21% and 18% of these states.

In Figures S2-S5, we examine how distortions away from the minimum-energy geometry of 2PhPy on S₀ affect the vertical excitation energy and oscillator strength of the $S_1 \leftarrow S_0$ transition. In particular, we sought to identify potential pathways for the Herzberg-Teller intensity borrowing for the $S_1 \leftarrow S_0$ transition. Figures S2 and S3 suggest that motions along $\phi_{ ext{scan}}$ and the NH wag do not significantly increase the oscillator strength of the $S_1 \leftarrow S_0$ transition. It is worth noting that decreasing ϕ_{scan} by approximately 10° from the minimumenergy geometry decreases $\Delta E_{S_1 \leftarrow S_0}$ from 36230 to 35778 cm⁻¹ while increasing $f_{S_1 \leftarrow S_0}$ from 0.006 to 0.008 au. Figure S4 shows that stretching the N-H bond causes an increase in $f_{S_1 \leftarrow S_0}$ and a decrease in $\Delta E_{S_1 \leftarrow S_0}$. Similarly, Figure S5 shows that distortions along the two CH wagging modes of the phenyl ring nearest the pyrrole ring cause an increase in $f_{S_1 \leftarrow S_0}$ and a decrease in $\Delta E_{S_1 \leftarrow S_0}$. The effect is largest when the CH wagging occurs at the CH bond that is oriented closest to the NH bond of the pyrrole. Overall, Figures S4 and S5 identify 2PhPy vibrational motions that significantly modulate $f_{S_1 \leftarrow S_0}$ and, hence, can facilitate Herzberg-Teller intensity borrowing. We therefore speculate that NH bond elongation and phenyl CH wagging increase the oscillator strength of the $S_1 \leftarrow S_0$

Turning to the S_1 state of 2PhPy, we performed unconstrained geometry optimizations on S_1 as well as developed a cut of the S_1 PES along ϕ_{scan} . The minimum-energy geometry

on S_1 is planar ($\phi_{scan} = 0^\circ$ and $\phi_{symm} = -89.97^\circ$). This contrasts with S_0 where the minimum-energy geometry is significantly nonplanar with $\phi_{scan} = 31.26^\circ$ and $\phi_{symm} = -58.34^\circ$. Figure S6 shows that the electronic characters of S_1 , S_2 , and S_3 at the S_1 -optimized geometry mirror those shown in Figure 2 for the S_0 -optimized geometry. Figures S7 and S8 present the results of a cubic spline interpolation through the electronic structure data that was constrained to be periodic. These figures show that the torsional potential is more confining on S_1 than on S_0 . In particular, the relative energy at the conformer where the rings are perpendicular ($\phi_{scan} = 90^\circ$ and $\phi_{symm} = -0.03^\circ$) is 771 cm⁻¹ on S_0 and 4918 cm⁻¹ on S_1 . As shown in Figure S9, the energy gap between the S_1 and S_2 states reaches a minimum value of 1708 cm⁻¹ at the S_1 -optimized planar geometry and increases as the ϕ_{scan} deviates from its optimal value.

Table S3 and Figures S10-S11 summarize the vertical excitation energies and associated NTOs at the So-optimized geometry of 2PhPy:1H₂O. As with 2PhPy, the $S_1 \leftarrow S_0$ transition is significantly multiconfigurational, exhibiting a combination of charge-transfer character, with electron density shifting onto the phenyl ring, and localized $\pi^* \leftarrow \pi$ character on the phenyl ring. The calculated vertical excitation energy and oscillator strength at the ADC(3)/aug-cc-pVDZ//CCSD/ jul-cc-pVDZ level of theory, $\Delta E_{S_1 \leftarrow S_0} = 36223 \text{ cm}^{-1}$ and $f_{S_1 \leftarrow S_0}$ = 0.009 au are very similar to the values obtained for 2PhPy. The $S_2 \leftarrow S_0$ transition has $\pi^* \leftarrow \pi$ character with the electron density delocalized across both rings, a larger vertical excitation energy of 37847 cm⁻¹, and a significantly larger oscillator strength of 0.405 au. The $S_3 \leftarrow S_0$ transition has $\sigma^* \leftarrow \pi$ character with $\Delta E_{S_3 \leftarrow S_0} = 39248 \text{ cm}^{-1} \text{ and } f_{S_3 \leftarrow S_0} = 0.006 \text{ au. As}$ with 2PhPy, the ordering of the excited states predicted by TD- ω B97X-D is inconsistent with that obtained from both the EOM-EE-CCSD and ADC(3). The S_0 – S_1 adiabatic energy gap calculated at the ADC(3)/jul-cc-pVDZ//CCSD/jul-cc-pVDZ level is 33329 cm⁻¹, representing a 635 cm⁻¹ decrease from

As with 2PhPy, we considered how distortions away from the S_0 -optimized geometry modulate $\Delta E_{S_1 \leftarrow S_0}$ and $f_{S_1 \leftarrow S_0}$. Similar to 2PhPy, if 2PhPy:1H2O distorts into a planar conformation ($\phi_{\text{scan}} = 0^{\circ} \text{ or } 180^{\circ}, \phi_{\text{symm}} = -90.11^{\circ} \text{ or } 89.83^{\circ},$ $E_{S_n} = 287.9 \text{ cm}^{-1}$), the $\Delta E_{S_1 \leftarrow S_0}$ and $\Delta E_{S_2 \leftarrow S_0}$ decrease modestly to 35311 and 36291 cm⁻¹, respectively. The conformation on S_0 with both rings perpendicular to one another ($\phi_{\text{scan}} = 90^{\circ}$, $\phi_{\text{symm}} = 1.34^{\circ}$, $E_{S_0} = 600.5 \text{ cm}^{-1}$) has larger vertical excitation energies, with $\Delta E_{S_1 \leftarrow S_0} = 39272$ cm⁻¹ and $\Delta E_{S_2 \leftarrow S_0} = 41556$ cm⁻¹. Both distortions along ϕ_{scan} cause $f_{S_1 \leftarrow S_0}$ to decrease from its value at the S₀-optimized geometry, 0.009 au. In contrast, Figure S12 shows that stretching the NH bond causes $\Delta E_{S_1 \leftarrow S_0}$ to decrease and $f_{S_1 \leftarrow S_0}$ to increase. Similarly, Figure S13 shows that wagging the CH bond on the phenyl ring closest to the pyrrole ring decreases $\Delta E_{S_1 \leftarrow S_0}$ and increases $f_{S_1 \leftarrow S_0}$. The analysis shown in Figures S12 and S13 suggests that, as for 2PhPy, Herzberg-Teller intensity borrowing driven by stretching the NH bond and wagging a CH bond on the phenyl increases the intensity of the $S_1 \leftarrow S_0$ transition.

As summarized in Figure S14, relaxation on S₁ has a significant effect on the electronic properties of 2PhPy:1H₂O. The vertical energy gap decreases from $\Delta E_{S_1 \leftarrow S_0} = 36223$ cm⁻¹ at the S₀-optimized geometry to $\Delta E_{S_1 \leftarrow S_0} = 29592$ cm⁻¹ at the

S₁-optimized geometry, consistent with a relatively large Stokes shift between absorption and fluorescence, 6,631 cm⁻¹. Interestingly, this is accompanied by a dramatic increase in the oscillator strength, with $f_{S_1 \leftarrow S_0} = 0.009$ au at the S_0 optimized geometry and $f_{S_1 \leftarrow S_0} = 0.171$ au at the S_1 -optimized geometry. At the S1-optimized geometry, the S1 \leftarrow S0 transition is much more dominated by the charge-transfer character than at the S₀-optimized geometry. It is worth noting that this differs markedly from that of 2PhPy, where geometry optimization on S_1 decreases $\Delta E_{S_1 \leftarrow S_0}$ by only 3847 cm⁻¹ and does not significantly affect $f_{S_1 \leftarrow S_0}$ or the electronic character of the S₁ state. Turning to the optimized geometry, unlike 2PhPy, the S₁-optimized geometry of 2PhPy:1H₂O remains nonplanar with one of the O-H bonds of H₂O directed toward the phenyl ring. Geometry relaxation on S₁ also induces out-ofplane distortions in both the NH bond and the CH bond on the phenyl ring that is closest to the NH bond. As a result, both bonds wag out-of-plane, so that they point away from each other. No such out-of-plane distortions were observed at the S_1 -optimized geometry of 2PhPy.

Experimental Results: UV Spectroscopy of 2PhPy: $n-H_2O$ (n=0-2) Microsolvated Complexes. The R2PI spectrum of 2PhPy is shown in Figure 3, revealing an

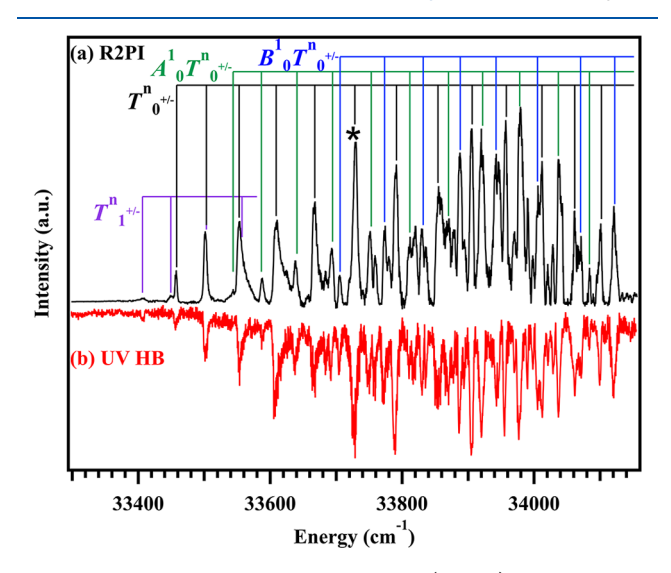


Figure 3. R2PI spectrum of 2-phenylpyrrole (2PhPy). The transitions labeled with black tie lines are assigned to the torsional mode progression $(T_0^{n_{\uparrow}-})$. The $A_0^1T_0^{n_{\uparrow}-}$ and $B_0^1T_0^{n_{\uparrow}-}$ combination band progressions are represented with the green and blue tie lines, respectively. The purple tie lines indicate "hot-band" transitions involving the torsional mode $(T_1^{n_{\uparrow}-})$.

electronic origin band at 33458 cm⁻¹ and vibronic structure spanning over 700 cm⁻¹ with significantly greater spectral density compared to 1-phenylpyrrole. The UV HB spectrum of 2PhPy is shown as an inverted red trace below the R2PI spectrum in Figure 3. The UV holeburn laser wavelength was fixed on the intense vibronic transition indicated by the asterisk in the figure. Other transitions were also used as the holeburn laser wavelength in separate experiments. Because each peak in the R2PI spectrum is accounted for in the UV HB spectrum, the results indicate that all vibronic transitions observed in the UV spectroscopy belong to a single 2PhPy conformational isomer. As indicated in Figure 3 with color-coded tie lines, there are four discernible vibronic progressions.

The progression transitions built off the electronic origin band (black tie lines) are separated on average by ~ 60 cm⁻¹, which is consistent with previous bichromophore studies 15,32,33 assigning the first series of peaks to the torsional mode between the pyrrole and phenyl rings. Similarly, we assign the progression labeled with the black tie lines to increasingly greater quanta in the excited electronic state torsional mode, $T_{0^{+/-}}^{n}$, from either $v'' = 0^{+}$ or $v'' = 0^{-}$ in the ground electronic state. The transition labeled with purple tie lines is assigned to a "hot-band" progression involving the torsional mode originating from $v'' = 1^{+/-}$, $T_{1^{+/-}}^n$. In principle, it is possible to separate transitions originating from $v'' = 0^{\pm}$ or $v'' = 1^{\pm}$ when using UV HB. Presumably, the transitions used for holeburning wavelengths included an overlap of vibronic features arising from levels with opposite symmetry. As seen in the ground state potential energy scan results in Figures S7 and S8, the torsional barrier separating the minima of 2PhPy is sufficiently large to form degenerate pairs from the torsional energy levels, resulting in states such as $T_{0^{+}}$ and $T_{0^{-}}$ that are symmetric and asymmetric, respectively, to the planar 2PhPy configuration. To observe the vibronic $T_{0^{+/-}}^n$ peaks in the R2PI excitation spectrum, the overall transition symmetry must be totally symmetric. Therefore, the peaks belonging to the $T_{0^{+/-}}^n$ vibronic progression are assigned as $T^0_{0^+}$, $T^1_{0^-}$, $T^2_{0^+}$, etc., because the ground state population will predominantly occupy the lowest vibrational levels as a result of supersonic jet cooling in the molecular beam. Shown in Figures S7 and S8, the calculated potential energy scans of 2PhPy indicate that the minimumenergy geometry, or more specifically the NC-CC dihedral angle, changes significantly in the ground and excited electronic states. This is in agreement with the Franck-Condon transition intensities observed in the R2PI spectrum of 2PhPy, where the peak intensity is greatest for $T_{0^{+/-}}^n$, n = 6

Two other vibronic progressions are tentatively assigned and color-coded in the R2PI spectrum, with similar energy differences between neighboring transitions ascribed to the torsional mode. The green and blue progressions shown in Figure 3 are identified as combination bands, assigned to $A_0^n T_{0^{+/-}}^n$ and $B_0^n T_{0^{+/-}}^n$, respectively. The $A_0^n T_{0^{+/-}}^n$ and $B_0^n T_{0^{+/-}}^n$ progressions indicate a series of combination bands resulting from the coupling between different vibrational modes (labeled A and B) with the torsional mode. In order for the A and B modes to couple with $T_{0^{+/-}}^n$, the vibronic transitions must be symmetry allowed.

The $A_0^n T_{0^{+/-}}^n$ progression in Figure 3 begins approximately +86 cm⁻¹ from the electronic origin, with each subsequent peak in the progression representing one additional quantum of energy in the torsional mode. The first six vibrational modes of 2PhPy are shown in Figure 4 which correlate to the S₂ electronic state at the TD-DFT ω B97X-D/6-311G++(d,p) level of theory; the S₂ state at the TD-DFT ω B97X-D/6-311G ++(d,p) level of theory has the same electronic character as the S₁ state shown in Figure 2. Plausibly, one quantum placed in the out-of-plane ring flapping vibrational mode (a'') calculated to be at 89 cm⁻¹ in Figure 4b may be assigned to the A mode because the criteria for the energy and overall totally symmetric transition symmetry would be met. In particular, excitation of the $A_0^1 T_{0^{+/-}}^n$ combination band progression involves simultaneous activation of the asymmetric a'' mode with an asymmetric torsional transition (e.g., $T_{0^+}^1$, $T_{0^-}^0$, $T_{0^-}^2$, $T_{0^-}^2$, etc.). Therefore, the combination bands labeled with $A_0^1 T_{0^{+/-}}^n$ are tentatively assigned as a progression involving one

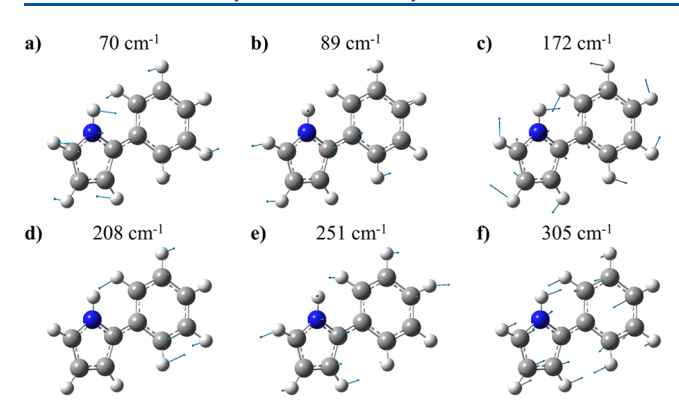


Figure 4. Theoretical predictions for the first six vibrational modes of 2PhPy in the S_2 electronic state at the TD-DFT ω B97X-D/6-311G++(d,p) level of theory; this has the same electronic character as the S_1 state in Figure 2. The nuclear displacement vectors are indicated with blue arrows.

quantum in an out-of-plane ring flapping mode coupled with $T_{0^{+}/-}^n$. The $B_0^n T_{0^{+}/-}^n$ progression begins approximately +248 cm⁻¹ away from the electronic origin. The calculated vibrational mode that is close in energy to 248 cm⁻¹ is the mode at 251 cm⁻¹ shown in Figure 4e. Therefore, the B mode is tentatively assigned to one quantum in this vibrational mode (a'') with out-of-plane nuclear motion of the CH and NH bonds. The progression is thus represented as $B_0^1 T_{0^{+}/-}^n$ with one quantum in the B mode with increasing quanta along $T_{0^{+}/-}^n$. The A and B mode assignments are supported by the analysis shown in Figure S5 where out-of-plane distortions of one of the CH bonds on the phenyl ring significantly affect $f_{S_0 \to S_1}$, potentially leading to Herzberg—Teller intensity borrowing.

Shown in Figure 5, the R2PI spectrum of the singly solvated 2PhPy:1 H_2O complex was obtained while monitoring the m/z = 161 mass channel with respect to the probe wavelength. Furthermore, the first several vibrational modes for 2PhPy:1- H_2O in its S_1 state from calculations are illustrated in Figure 6.

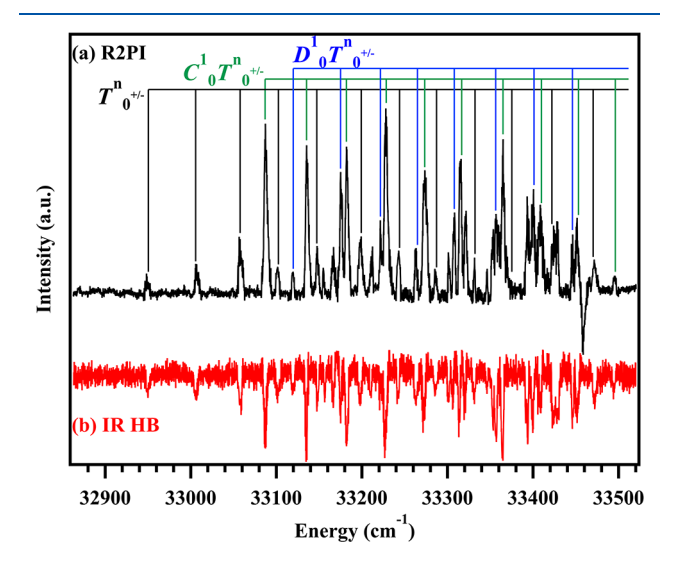


Figure 5. R2PI spectrum of 2-phenylpyrrole with a single water molecule (2PhPy:1H₂O). The black tie lines signify transitions due to the torsional mode progression $(T^n_{0^{+/-}})$, and the green and blue tie lines indicate the $C^1_0T^n_{0^{+/-}}$ and $D^1_0T^n_{0^{+/-}}$ combination band progressions. The negative-going peak at 33458 cm⁻¹ corresponds to the electronic origin of the 2PhPy parent molecule.

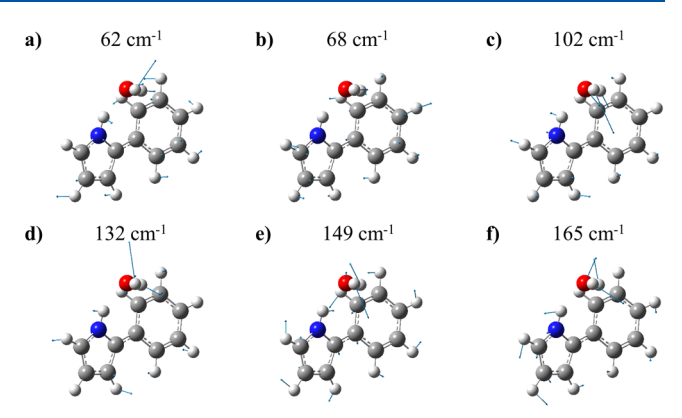


Figure 6. Theoretical predictions for the first six vibrational modes of 2PhPy:1H₂O in the S_2 electronic state at the TD-DFT ω B97X-D/6-311G++(d,p) level of theory; this has the same electronic character as the S_1 state in Figure S10. The nuclear displacement vectors are indicated with blue arrows.

The electronic origin band is located at 32948 cm⁻¹, redshifted from the bare chromophore electronic origin by -510cm⁻¹ due to microsolvation with water. Our computational approaches overestimate this red-shift by 125 cm⁻¹. The R2PI spectrum of 2PhPy:1H₂O is similar to that of 2PhPy with a Franck-Condon intensity profile involving the torsional mode, $T_{0^{+/-}}^{n}$ and two combination band progressions, labeled with black, green, and blue tie lines, respectively. The interval between adjacent transitions for the $T_{0^{+/-}}^n$ progression is approximately 55 cm⁻¹, which agrees with the predicted lowest-frequency torsional mode at 62 cm⁻¹ shown in Figure 6. Furthermore, the torsional mode progression in the R2PI spectrum of the 2PhPy:1H₂O complex is lower in intensity relative to the other vibronic progressions. However, the torsional mode progression has the strongest intensity profile in the R2PI spectrum of the bare 2PhPy chromophore in Figure 3. The additional progressions shown with green and blue tie lines in Figure 5 are assigned to combination bands with the torsional mode $C_0^n T_0^{n_{+}/-}$ and $D_0^n T_0^{n_{+}/-}$, respectively. The $C_0^n T_0^{n_{+}/-}$ progression appears at +138 cm⁻¹ from the electronic origin band, while it is observed that the $D_0^n T_{0^{+/-}}^n$ progression starts at +170 cm⁻¹. Because of the asymmetry from water complexation to 2PhPy, the transition symmetry selection rules are somewhat more relaxed. There is a predicted vibrational mode at 132 cm⁻¹ seen in Figure 6d, which resembles a torsional motion with significant out-of-plane motion of the CH and NH bonds. Indeed, the N-H bond is out of the plane with respect to the rest of the pyrrole ring following electronic excitation of 2PhPy:1H2O. This is consistent with the out-ofplane distortion of one of the CH bonds of phenyl during vibrational relaxation on S₁, as well as the analysis shown in Figure S13. Therefore, it is possible that the transitions belonging to the $C_0^n T_0^{n+/-}$ progression arise from coupling between one quantum in the predicted 132 cm⁻¹ vibrational mode (C_0^1) and $T_{0^{+/-}}^n$. Furthermore, we tentatively assign the progression denoted with blue tie lines as $D_0^1 T_{0^{+/-}}^n$, which involves a series of transitions with a single quantum in the D vibrational mode at 165 cm⁻¹ (Figure 6f) and $T_{0^+/-}^n$. Qualitatively, the mode at 165 cm⁻¹ can be described as the two aromatic rings undergoing an in-plane scissoring motion, which is consistent with C-C bond compression upon excitation of the 2PhPy chromophore (see Table S4).

Using the infrared transition found at 3423 cm⁻¹ as the holeburn laser wavelength and scanning the probe laser, we obtained the IR HB spectrum for 2PhPy:1H₂O shown as the inverted red trace in Figure 5. As indicated in the figure, because all transitions are present, we determined that only a single conformational isomer for the 2PhPy:1H₂O molecular complex exists under our experimental conditions. The R2PI spectrum of 2PhPy:2H₂O (m/z=179) is presented in Figure S16, albeit with less signal-to-noise, which we attribute to small ground state populations and/or photochemical dynamics upon electronic excitation.

Experimental Results: IR Spectroscopy of 2PhPy: $n-H_2O$ (n=0-3) Microsolvated Complexes. Figure 7 shows

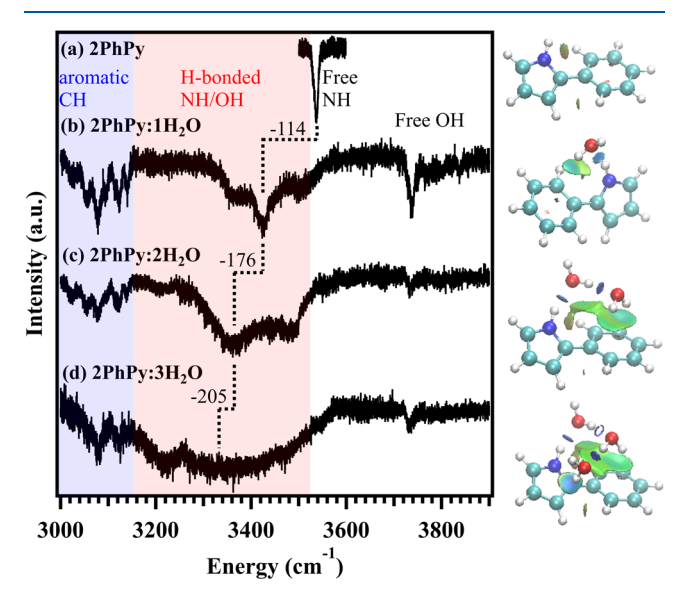


Figure 7. Ground state infrared spectra of 2PhPy:nH₂O (n = 0–3) from 3000 to 3900 cm⁻¹. Resonant ion-depletion infrared (RIDIR) spectra are shown for (a) 2PhPy and (b) 2PhPy:1H₂O, and nonresonant ion-depletion infrared (nRIDIR) spectra are shown for (c) 2PhPy:2H₂O and (d) 2PhPy:3H₂O. The RIDIR spectrum for 2PhPy:2H₂O is shown in Figure S17. The infrared spectra are divided into three color-shaded regions: aromatic CH stretch (blue), hydrogen-bonded NH or OH stretch (red), and free NH or OH stretch (unshaded). The right column displays the lowest-energy conformational isomers of 2PhPy:nH₂O (n = 0–3) at the ωB97X-D/6-311G++(d,p) level, along with the intermolecular interactions superimposed as color-coded isosurfaces on the structures. The blue, green, and red isosurfaces represent strong hydrogen bonding, weak van der Waals interactions, and repulsive interactions, respectively.

the IR spectra for $2PhPy:nH_2O$, n=0-3, from 3000-3900 cm⁻¹. RIDIR spectra were collected for $2PhPy:nH_2O$, n=0-2, when the UV probe laser wavelength was resonant on a UV transition (33729, 33228, and 33070 cm⁻¹, respectively). The RIDIR spectrum for $2PhPy:2H_2O$ is presented in Figure S17. Furthermore, the IR spectra for $2PhPy:nH_2O$, n=2-3 were obtained using the nRIDIR spectroscopy technique, in which the UV probe laser was not fixed on a resonant transition. Each vibrational transition observed in the RIDIR spectrum of $2PhPy:2H_2O$ is accounted for in the nRIDIR spectrum, thus indicating a single conformational isomer and minimal complex ion fragmentation from larger complexes. A comparison between the RIDIR and nRIDIR spectra of $2PhPy:2H_2O$ is shown in Figure S17. Despite an extensive search, no resonant UV transitions were found for the

2PhPy:3H₂O complex due to a small degree of signal and/or photochemical dynamics upon electronic excitation. Thus, only the nRIDIR spectrum is shown in Figure 7.

The IR spectra are divided into three spectral wavelength regions, which are differentiated by the hydride stretch by using color-coded shading. In particular, the aromatic CH stretch and hydrogen-bonded NH or OH stretch regions are distinguished with blue and red shading, respectively, while the free NH or OH stretch region does not have shading. Between 3000 and 3150 cm⁻¹, the CH stretch modes belonging to either the pyrrole or phenyl ring are observed, whereas the free OH stretches for the water solvent partners appear between $\sim\!3700$ and 3850 cm⁻¹. As seen for the bare 2PhPy chromophore in Figure 7, the free NH stretch is located at 3537 cm⁻¹. Upon stepwise addition of water solvation, the intermolecular interactions between 2PhPy and $\rm H_2O$ are anticipated to be encoded in the IR spectroscopy.

The right-hand column of Figure 7 illustrates the non-covalent interactions present within the 2PhPy: nH_2O (n=0-3) complexes determined using NCIPlot. ³⁴ Where the reduced density gradient (RDG; $s(\rho)$) vanishes in regions with low electron densities (ρ), this approach generates isosurfaces to visualize the strength of the noncovalent bonding patterns between nuclei. Thus, the intermolecular interactions between solute and solvent partners can be analyzed via electron density singularities, in which the second Hessian eigenvalue (λ_2) signs determine the noncovalent interaction class and the interaction strength is obtained from ρ . The isosurfaces imprinted on the optimized ground state geometries in the figure display favorable hydrogen-bonding (blue), van der Waals (green), and repulsive interactions (red).

Between the $\sim 3150-3520~\rm cm^{-1}$ spectral range highlighted with red shading in Figure 7, vibrational transitions associated with the hydrogen-bonded NH or OH stretches of the 2PhPy: nH_2O (n=1-3) complexes are present. In this region, the RIDIR spectrum of the singly solvated 2PhPy: H_2O complex displays three transitions, the most intense of which is tentatively assigned to the hydrogen-bonded NH stretch of the 2PhPy chromophore. As can be seen from the NCI isosurfaces to the right of the 2PhPy: H_2O RIDIR spectrum, 2PhPy acts as a hydrogen-bond donor to the adjacent H_2O acceptor with the strong interaction distinguished with a blue isosurface. This noncovalent interaction results in a red-shifting of the NH stretch by approximately $-114~\rm cm^{-1}$ with respect to the free NH stretch of 2PhPy, appearing at $\sim 3423~\rm cm^{-1}$.

As two H_2O solvent partners interact with 2PhPy, the initial hydrogen-bonding motif is maintained between the pyrrole ring donor and the nearest H_2O acceptor as observed for 2PhPy:1 H_2O . Now with two H_2O molecules in the complex, the NCIPlot results indicate that the hydrogen bonding is cooperatively strengthened as the water network forms a bridge between the pyrrole and phenyl rings. Indeed, the hydrogen atoms from the additional H_2O interact with the phenyl ring π system through van der Waals forces in the form of a H atom/ π interaction. Subsequently, the NH stretch of 2PhPy:2 H_2O tentatively assigned to the 3361 cm⁻¹ peak decreases by -176 cm⁻¹ from the free NH stretch of 2PhPy. Furthermore, the free OH stretch is observed at 3719 cm⁻¹.

The bottom panel in Figure 7 shows the IR spectrum of $2PhPy:3H_2O$, with the lowest-energy conformational isomer shown with NCI isosurfaces in the right panel. In a similar fashion to the smaller complexes, the water network extends between both aromatic rings, with the last H_2O molecule

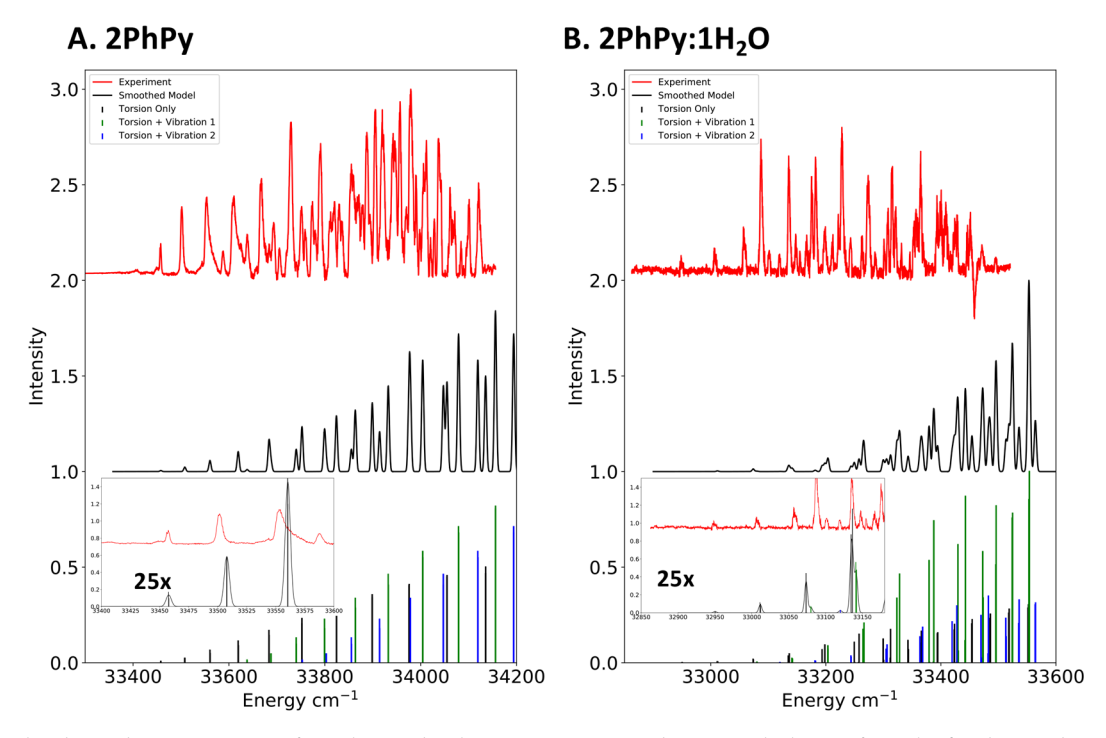


Figure 8. Simulated UV absorption spectra for 2PhPy and 2PhPy:H₂O using periodic DVR calculations from the fitted ground state and excited state torsional potentials. Relative intensities were assumed to be proportional to the square of the overlap of the calculated wave functions from the DVR calculations.

returning to the pyrrole unit through a moderately strong H atom/ π interaction. Portrayed in the figure, the strong hydrogen-bonding H₂O network accommodates the 2PhPy chromophore through a 5-membered configuration. Strikingly, the IR spectrum of 2PhPy:3H₂O is significantly broadened, appearing as a structureless feature starting from 3150 cm⁻¹ and ending approximately at 3575 cm⁻¹. The hydrogenbonded NH stretch is tentatively assigned near the middle of the feature at 3333 cm⁻¹, red-shifted by -205 cm⁻¹ to a lower energy relative to that of 2PhPy. The Supporting Information contains the calculated harmonic vibrational spectra of each $2PhPy:nH_2O$ (n = 0-3) complex at the $\omega B97X-D/6-311G+$ +(d,p) level. As will be discussed in more detail in the Discussion section, the hydrogen-bonded OH stretches belonging to the H₂O solvent partners and the NH wagging and HOH bending modes are predicted to be nearby in energy to the hydrogen-bonded NH stretches, likely complicating the IR spectra through anharmonic coupling.

DISCUSSION

Excited Electronic State Photophysical Outcomes.

The simulation of the electronic spectra with periodic DVR calculations is shown in Figure 8. Similar to the work with 1-phenylpyrrole (1PhPy),¹⁵ fitting the spectrum requires adding two additional torsional progressions with shifted origins, consistent with the interpretation in the experimental results section. However, for these molecules, the intensities for the lowest energy transitions are generally underestimated compared to the experiment (see the inset of Figure 8b). The estimated intensities of these lowest transitions are quite sensitive to the torsional wave functions, and small changes in the potential energy surface could lead to large relative changes in the intensities. Despite these weaknesses, the energy level structure of the torsional progression is generally in agreement

with experiment (a full list of transitions are provided as csv files and are available on the GitHub repository).

Though the electronic structure of 2PhPy (and 2PhPy:1-H₂O) has complicated excited state surfaces, there are some similarities in the overall behavior of their electronic spectra to the 1PhPy and 1PhPy:1H₂O cases. The ground state torsional potential energy surface for 1PhPy has nearly equal barrier heights of 500 cm⁻¹ for each of the torsional barriers. In contrast, the 2PhPy ground state has a sharper contrast between the higher and lower barriers (791 and 127 cm⁻¹). In both cases, the barrier heights are high enough to produce a quartet of nearly degenerate states. The excited state barrier (mentioned above) is much higher for 2PhPy than for 1PhPy (nearly 5000 cm⁻¹ compared to 1200 cm⁻¹). In addition, the torsional wells are much broader. For 2PhPy:1H2O the ground state torsional potential is qualitatively similar to that of 1PhPy:H₂O; however, in this case the 2PhPy:1H₂O has a sharper contrast in barrier heights on the ground state than the 1PhPy:1H₂O case, where each of the barriers are similar. The excited state torsional potential for 2PhPy:1H₂O is qualitatively different than 1PhPy:1H₂O—in this case 2PhPy:1H₂O has more local minima along the torsional coordinate than 1PhPy:1H₂O, and the minima (as a function of angle) between the ground and excited state are more closely aligned than 1PhPy:1H₂O. This directly leads to more bright transitions (compared to 1PhPy:1H₂O), which also captured in the theoretical spectra.

The 2PhPy chromophore represents an extended π -conjugated pyrrole derivative, and its excited electronic state pathways have been explored in this work by using experimental and theoretical methods. To gain additional insights into the outcomes following electronic activation of 2PhPy, we now turn the discussion to comparisons with the photoinitiated dynamics of the bare pyrrole monomer and complexes made between pyrrole and other molecular

partners. Previous studies have characterized the excited state photophysical and photochemical mechanisms of pyrrole³⁵, and pyrrole complexes with itself and with water microsolvation. 12,37 It is well-documented that the pyrrole monomer undergoes ultrafast, photochemical H atom dissociation due to nonadiabatic coupling of the $\pi^* \leftarrow \pi$ bright state with a $\sigma^* \leftarrow$ π state. More recently, both experimental and theoretical efforts have focused on the charge transfer pathways between pyrrole dimers and pyrrole complexes with water.^{37–40} Upon UV photoactivation of pyrrole complexes, a nonnegligible degree of electron charge is transported from the pyrrole donor π -system to either the pyrrole or the water acceptor(s). The extent of charge transferred to the surrounding solvation environment and hence the formation of the hydrated electron have important photochemical consequences, particularly at aerosol interfaces. 7,14 Notably, activation of pyrrole along the NH bond facilitates both vibronic coupling between excited electronic states and the control of charge transfer to the solvation environment.

As illustrated in Figure 2, the S₁ electronic state of 2PhPy has mixed character: charge transfer from the pyrrole to the phenyl ring (twisted intramolecular charge transfer, TICT) and localized $\pi^* \leftarrow \pi$ excitation on the phenyl ring (locally excited state, LE). Furthermore, the $S_1 \leftarrow S_0$ transition oscillator strength is small while the $S_2 \leftarrow S_0$ transition is optically bright. As discussed in Figures S2-S5, the $S_1 \leftarrow S_0$ transition gains intensity through distortions involving the CH wagging motion on the phenyl ring closest to the pyrrole ring and stretching of the NH bond. Furthermore, Figure S19 shows that upon stretching the NH bond length to 1.16 Å on S₁, the electronic character of the S_1 state changes dramatically from $\pi^* \leftarrow \pi$ to $\sigma^* \leftarrow \pi$. As this occurs, the S₁ potential flattens along the NH stretch coordinate. Similar to the picture of pyrrole photochemistry developed by Domcke and co-workers, this analysis suggests that an initial $\pi^* \leftarrow \pi$ excitation can develop $\sigma^* \leftarrow \pi$ character which facilitates NH bond breaking. 12 We speculate that the abrupt termination of the 2PhPy R2PI spectrum shown in Figure 3 reflects the photolysis of the NH bond. The presence of a barrier preceding NH bond breaking shown in Figure S19 is consistent with the S₁ state of 2PhPy having a sufficiently long lifetime to produce a R2PI spectrum when the vibrational energy on S_1 is relatively low.

The 2PhPy:1H₂O system exhibits significant similarities and differences from 2PhPy. Comparing Figures 2 and S9, we see that the $S_2 \leftarrow S_0$ transition of both systems is much brighter than the $S_1 \leftarrow S_0$ transition. However, vibrational relaxation on S₁ for 2PhPy:1H₂O results in out-of-plane distortions involving the NH bond and the CH bond on the pyrrole nearest to the phenyl ring. This is associated with a significant Stokes shift and increase in intensity. Figures S12 and S13 show that stretching the NH bond and/or wagging the CH bond on the phenyl ring closest to the NH bond of pyrrole cause an increase in the intensity of the $S_1 \leftarrow S_0$ transition, suggesting that distortions along this vibrational mode help to drive the S₁ \leftarrow S₀ transition. Based on this and the analysis shown in Figure S19 for 2PhPy, we postulate that NH bond photolysis results in the abrupt termination of the R2PI spectrum of 2PhPy:1H₂O observed in Figure 5. Moreover, following Domcke and co-workers, the development of $\sigma^* \leftarrow \pi$ character in S_1 could facilitate charge transfer to the solvent. 12 A detailed analysis of the photochemistry of 2PhPy and 2PhPy:1H₂O is outside the scope of this study and is an active area of investigation in our laboratories.

The gas-phase 2PhPy:nH₂O results mimic the intermolecular interactions and partial solvation configurations at the aerosol air/water interface. Consequently, the photophysical outcomes from solar absorption may be different at the interface compared to the fully solvated environment closer to the interior of the aerosol. To this end, condensed-phase UV absorption and fluorescence emission studies were performed with 2PhPy dissolved in a series of % volume THF:H₂O. Shown in Figure 9, the UV absorption spectrum of 2PhPy in

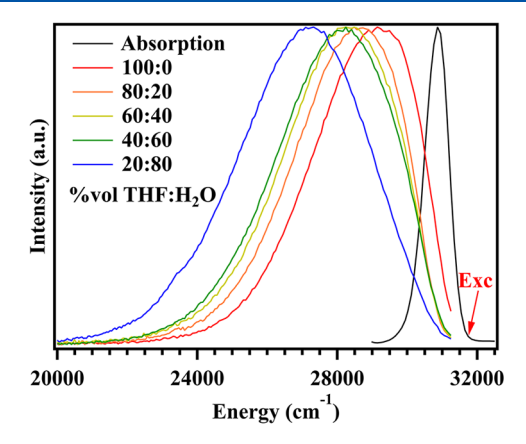


Figure 9. Absorption (black trace) and color-coded fluorescence spectra of 2PhPy in tetrahydrofuran (THF) with increasing % volume of water ($\rm H_2O$), indicated with % volume THF: $\rm H_2O$. The excitation wavelength used during fluorescence experiments was 315 nm with samples kept at 25 °C.

100% volume THF begins approximately at 29300 cm⁻¹, with a maximum at 30900 cm⁻¹ and a full width at half-maximum of 800 cm⁻¹. Using this same sample with an excitation wavelength of 31746 cm⁻¹ (315 nm), the corresponding fluorescence emission spectrum is shown as a red trace in the figure. Notably, the 2PhPy emission spectrum in 100% volume THF peaks at 29150 cm⁻¹, along with a full width at half-maximum of 3650 cm⁻¹, and is tentatively assigned to the $\rm S_2$ state with $\pi\pi^*$ character.

As listed in Table 1, the peak emission wavelength continues to decrease with increasing % volume H_2O , with a concomitant

Table 1. Emission Feature Characteristics from 2-Phenylpyrrole in a Series of % Volumes of Tetrahydrofuran and Water

% volume THF:H ₂ O	peak emission energy (cm^{-1})	$\begin{array}{c} \text{full width at half-maximum} \\ \text{(cm}^{-1}) \end{array}$
100:0	29150	3650
80:20	28500	3750
60:40	28350	3950
40:60	28250	4150
20:80	27300	4500

increase in the full width at half-maximum. In particular, for the 20:80% volume THF: $\rm H_2O$ sample shown as the blue trace in Figure 9, the emission wavelength reaches a maximum at 27300 cm⁻¹ and a full width at half-maximum of 4500 cm⁻¹. This red-shift in the emission spectra is consistent with the electronic origin band and vibronic transitions decreasing to lower energy in the R2PI spectra of the gas-phase 2PhPy: $\rm nH_2O$ molecular complexes. For the 20:80% volume THF: $\rm H_2O$ sample, a shoulder emission band at ~23500 cm⁻¹ was

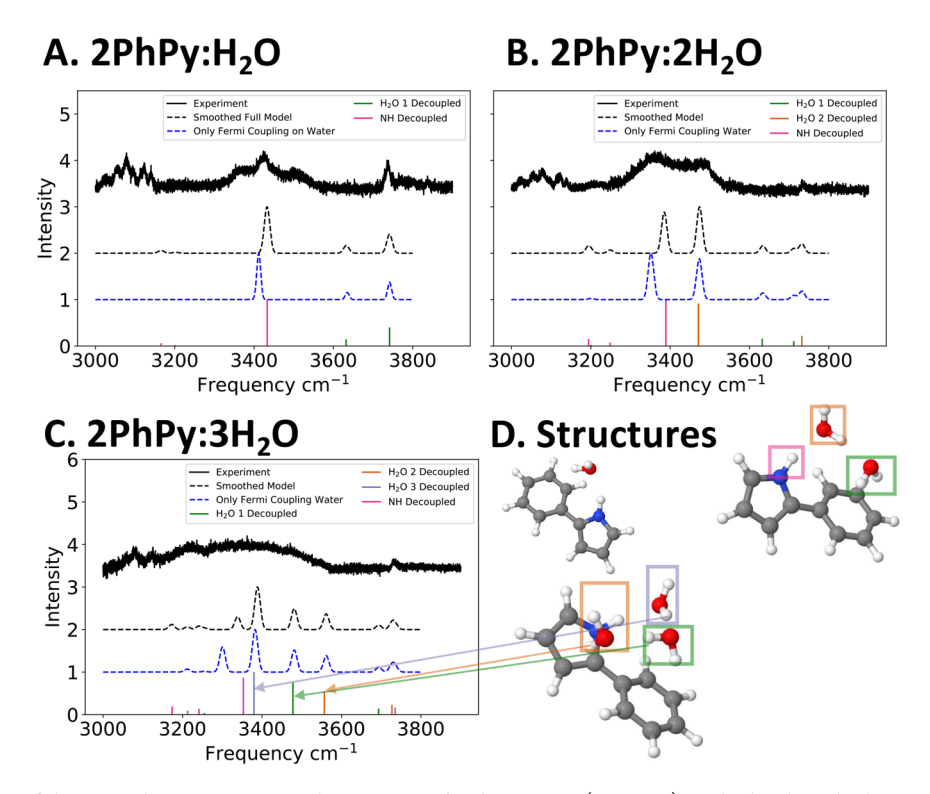


Figure 10. Comparison of the ground state experimental IR spectra of $2PhPy:nH_2O$ (n = 1-3) to the local mode theoretical model. Local mode Hamiltonian matrices are provided in Figures S20-S22. The bottom of each plot shows the spectrum that is obtained if intramolecular coupling is turned off between each water (and the 2PhPy NH modes).

observed and is tentatively assigned to the S_1 state. According to calculations, the addition of a single water molecule hydrogen-bonded to 2PhPy causes significantly greater vibrational relaxation (\sim 6600 cm⁻¹ for 2PhPy:1H₂O versus 3850 cm⁻¹ for 2PhPy). Furthermore, the oscillator strength increases substantially upon single H₂O solvation, wherein the oscillator strength rises from 0.009 au to 0.171 au. This physical picture agrees qualitatively with the observation that the fluorescence shifts to lower energy with increasing amounts of water, in addition to the S_1 state appearing at lower energy due to an increase in its oscillator strength.

Ground Electronic State 2PhPy:NH₂O Conformational Isomers. Figure 10 shows the IR spectroscopy results using the local mode Hamiltonian theoretical model. As shown in the figure for the 2PhPy:1H₂O complex, the stretching frequencies are sufficiently high that they do not couple to the scissor overtone of the water. The addition of two NH wagging modes into the model only makes a modest effect on the spectrum (difference between the black and blue traces). Thus, the splitting of the NH stretch peak in the 2PhPy:1H₂O IR spectrum is not due to simple Fermi resonance interactions but instead comes from other effects. The vibrational peak may be split by coupling to the torsional modes.²⁹

In the 2PhPy: $2H_2O$ complex, the two main features between 3400 and 3600 cm⁻¹ can be attributed to the NH stretch (and coupled wagging modes) and the hydrogen-bonded OH group in the water that accepts a hydrogen bond from the NH in 2PhPy. The peak associated with the NH stretch is pushed slightly higher in frequency by the coupling to the NH wagging mode overtones (see the difference between the blue and black spectra in Figure 10b), and the small peak seen in the experimental spectrum at 3200 cm⁻¹ can be tentatively

attributed the NH wagging overtones borrowing intensity from the stretch.

Although the interaction of OH stretches with π -systems (in this case, phenyl systems) is weaker than H-bonding interactions, the presence of both the phenyl and pyrrole π clouds enables the formation of a noncyclic trimer cluster (in 2PhPy:3H₂O), which involves hydrogen bonding of the NH, and then π -interactions with the pyrrole ring on the other end. The dihedral angles between the phenyl and pyrrole ring also change slightly, by about 6° (toward being more coplanar), from the 1H₂O to 3H₂O complex. In the 2PhPy:3H₂O complex, the spectrum is substantially broadened, so although the coupling between the stretches and the wagging and scissor overtones in the model Hamiltonian gives approximately the correct span of the frequencies, the additional effects that lead to the broadening of the spectrum are not captured with this model and make the definitive evaluation of the predicted frequencies and intensities difficult.

In Figures S20–S22, we provide the local mode Hamiltonians, which provide an intuitive picture for evaluating the relative strength of the hydrogen-bonding interactions in the complexes. The results show that the lowest frequency NH stretch is in the 2PhPy:3H₂O complex. For both the 2PhPy:2H₂O and 2PhPy:3H₂O complexes, the NH stretch mixes with the local mode OH stretches. This can be seen through two methods. First, at the local mode level, the couplings between the NH and nearest-neighbor—water local OH stretches increase from being less than 10 cm⁻¹ (in magnitude) in the 2PhPy:1H₂O complex to being 20 and 27 cm⁻¹ in the 2PhPy:2H₂O and 2PhPy:3H₂O complexes, respectively. To put this coupling in context, this degree of intermolecular coupling is on the same order as the *intra*molecular coupling seen in double-donor waters in larger

(e.g., hexamer) pure water clusters. Second, the intermolecular stretch—stretch coupling can be turned off, making the local mode Hamiltonian block diagonal for each water (and NH) which results in the individual peaks being directly attributable (impulse plots at the bottom of Figure 10a—c). When there are substantial shifts in the coupled and uncoupled spectra, we conclude that the spectra should be interpreted as the result of mixing between different stretching modes. Although the 2PhPy:3H₂O infrared spectrum was recorded using a nonresonant ion-depletion method, the local mode Hamiltonian results agree well with the overall shape of the vibrational features. However, this does not exclude the possibility that minor 2PhPy:3H₂O conformational isomers may contribute to the infrared spectrum.

The local solvation environment in aerosols plays a major role in the configuration of solute chromophores and, therefore, the accessible photophysical and photochemical outcomes. Because the pyrrole subunit is pervasive in areas spanning biology to materials to aerosols, previous theoretical and experimental spectroscopy studies have been performed to characterize the microsolvated pyrrole complexes with water. 42-44 Wu and co-workers 42 utilized cavity-based and chirped pulse Fourier transform microwave spectroscopy to determine structural information on the pyrrole:1H2O molecular complex. The authors determined that the hydrogen-bonded pyrrole:1H2O complex is the most energetically favorable conformational isomer with the pyrrole H atom donor directly oriented to the O atom acceptor of H2O, wherein the H atoms are out-of-plane of the pyrrole ring. Furthermore, infrared spectroscopy studies have been performed by Matsumoto⁴³ and Sarkar⁴⁴ to further reveal the pyrrole:nH2O microsolvated structures. Matsumoto et al. applied infrared cavity ring-down spectroscopy and quantum chemical calculations to observe the NH and OH stretching vibrations of the pyrrole:1H2O complex. Here, they observed the free NH stretch of the pyrrole monomer at 3531 cm⁻¹ and the hydrogen-bonded NH stretch from pyrrole:1H₂O at 3448 cm⁻¹. Sarkar et al. used nitrogen matrix infrared spectroscopy to determine the NH stretches of pyrrole:1H2O and pyrrole:2H₂O to be 3385 and 3409 cm⁻¹, respectively. Furthermore, both infrared studies found a similar pyrrole:1-H₂O structure as Wu, and Sarkar concluded that the nearest water oriented toward the NH bond is out-of-plane to form a hydrogen bond with the second water molecule. Interestingly, the second water molecule in the pyrrole:2H₂O complex forms a stabilizing π -H atom interaction with the pyrrole ring.

Shown in Figure 7, the free NH stretch of the bare 2PhPy chromophore is located at 3537 cm⁻¹, which is in agreement with the value for pyrrole reported by Matsumoto. Forming 2PhPy:1H₂O and 2PhPy:2H₂O with sequential water addition, the hydrogen-bonded NH stretches were found at 3423 and 3361 cm⁻¹, respectively, in Figure 7. The agreement between the NH stretch vibration of 2PhPy:1H₂O in the present study and those from previous infrared studies of pyrrole:1H2O is generally good. This is plausibly due to similar configurations, where the O atom of H₂O for 2PhPy:1H₂O is directed toward the NH bond of the pyrrole ring with the out-of-plane H atoms interacting with the neighboring phenyl π -system via van der Waals forces. For 2PhPy:2H2O, the second H2O molecule forms a van der Waals interaction with the phenyl ring as opposed to pyrrole:2H2O, where the second H2O interfaces with the pyrrole ring. It is not until 2PhPy:3H₂O that the last H_2O forms a stronger π/H atom stabilization with the pyrrole ring, similar to pyrrole: $2H_2O$. As illustrated in the right column of Figure 7, stepwise H_2O addition for the $2PhPy:nH_2O$ (n=0-3) complexes results in the NH bond increasing from 1.005, 1.014, 1.019, and 1.022 Å from cooperativity effects. It is likely that the extent of anharmonic coupling increases for the $2PhPy:nH_2O$ complexes as a result of NH bond elongation. This is consistent with the relative broadening of the IR spectra, in addition to the anharmonicity constants from the local mode Hamiltonian simulations.

It is also worth comparing the results reported in this study with those found by Carney and Zwier for indole:nH2O.45 Indole consists of fused benzene and pyrrole rings, whereas 2PhPy has the phenyl group appended to pyrrole. Both systems exhibit similar hydrogen bonding motifs, with the initial water molecule hydrogen bonding with the NH bond and subsequent water molecules forming a hydrogen-bonding chain. The terminal water molecule in this chain interacts with the π -system of the chromophore. RIDIR spectra of indole:nH2O revealed that the N-H stretch shifts to lower frequencies with the sequential addition of water molecules. Moreover, for indole:2H₂O, the N-H stretching mode becomes coupled with the O-H stretching modes of water molecules in the chain. Similar trends are observed in the 2PhPy:nH2O data collected in this study. Overall, we see that pyrrole:nH₂O, indole:nH₂O, and 2PhPy:nH₂O systems exhibit similar hydrogen-bonding motifs, the effects of which imprint themselves in similar ways within the vibrational spectra of the microhydrated complexes.

CONCLUSION

Using a synergy of experimental and theoretical methods, this study explored the conformational isomers and solar absorption mechanisms of water microsolvated 2-phenyl-pyrrole (2PhPy:nH₂O) complexes on a single-conformation basis. The molecular geometries of the complexes shape accessible photophysical and photochemical outcomes. Using conformation-specific infrared spectroscopy, the 2PhPy:nH₂O structures investigated in this work mimic the partially solvated environment of BrC chromophores at the air/water interface. Furthermore, characterizing the ultraviolet spectroscopy and dynamics of 2PhPy:nH₂O complexes with single-conformation specificity yields insights into the solar processing of BrC aerosol interfaces at the molecular level.

To this end, vibronic progressions and combination bands involving the torsional mode were observed in the resonant two-photon ionization (R2PI) spectra of 2PhPy and 2PhPy:1H₂O. An abrupt termination of resonant transitions in the spectra was speculated to arise from a switching of the S₁ electronic state character from $\pi^* \leftarrow \pi$ to $\sigma^* \leftarrow \pi$ at elongated NH bond lengths, which facilitates photolysis of the NH bond. Using double-resonance holeburning methods, a single conformational isomer was found for 2PhPy and 2PhPy:1H₂O, therefore indicating that all transitions belonged to a unique geometry. Therefore, the torsional and combination band progressions were simulated using torsional potential surfaces at the MP3 (ground state) and ADC(3) (excited state) levels of theory in tandem with discrete variable representation to obtain the simulated transition frequencies and intensities. The agreement between the experimental and theoretical ultraviolet spectra revealed the torsional barriers to intramolecular charge transfer between the pyrrole donor and phenyl ring π -systems, which were affected by the noncovalent interactions with a hydrogen-bonding H₂O molecule. Furthermore, theoretical

calculations also suggest that distortions along out-of-plane phenyl CH wagging modes and the NH stretching mode induce Herzberg—Teller vibronic coupling, increasing the intensity of the $S_1 \leftarrow S_0$ transition. Consequently, the vibronic intensity profile substantially increases for the 2PhPy:1H₂O combination band progression involving the torsional mode and an out-of-plane phenyl CH wagging mode compared with 2PhPy.

Additionally, conformation-specific infrared spectra reported on the intermolecular interactions and conformational isomer configurations of 2PhPy:nH2O. With increasing H2O microsolvation, the hydrogen-bonding morphology forms an extended network across the pyrrole and phenyl aromatic rings. In particular, a noncovalent interaction is formed between the NH bond of pyrrole and the nearest H₂O partner. Building the local solvation environment surrounding 2PhPy, the second H₂O bridges both aromatic rings with a hydrogen bond with the first H₂O molecule while also interacting with the phenyl ring through a π/H atom stabilization. Likewise, the third H₂O forms a hydrogen bond with the second H_2O ; however, a moderately strong π/H atom interaction takes place with the pyrrole ring. Therefore, a fivemembered configuration forms between the 2PhPy solute and the H₂O solvation wire. With sequential addition of H₂O solvation, the likelihood that anharmonic coupling may play a role increases. A local mode Hamiltonian approach was utilized to interpret the infrared spectra, thus assigning the vibrational transitions to individual oscillators in the 2PhPy:nH2O molecular complexes. The local mode harmonic coupling constants for NH and the nearest H2O local OH stretches were found to increase for 2PhPy: nH_2O (n = 1-3). Significant spectral broadening is observed in the infrared spectra going from one to three H₂O molecules incorporated in the complexes, possibly pointing to a dynamical effect between the 2PhPy solute and the H₂O solvation network.

ASSOCIATED CONTENT

Supporting Information

The Supporting Information is available free of charge at https://pubs.acs.org/doi/10.1021/acs.jpca.3c04472.

Excited electronic state computational results for 2PhPy and 2PhPy:1H₂O, potential energy surfaces for 2PhPy and 2PhPy:1H₂O used in the DVR simulations, ground and excited electronic state bond lengths of 2PhPy and 2PhPy:1H₂O, R2PI, RIDIR, and nRIDIR spectra of 2PhPy:2H₂O, IR spectra of 2PhPy:*n*H₂O compared to harmonic calculations, S₁ electronic state character of 2PhPy as a function of NH bond length, local mode Hamiltonians for 2PhPy:*n*H₂O (PDF)

AUTHOR INFORMATION

Corresponding Authors

Nathanael M. Kidwell — Department of Chemistry, The College of William & Mary, Williamsburg, Virginia 23187-8795, United States; orcid.org/0000-0002-7065-4486; Email: nmkidwell@wm.edu

Daniel P. Tabor — Department of Chemistry, Texas A&M University, College Station, Texas 77843, United States; orcid.org/0000-0002-8680-6667; Email: daniel_tabor@tamu.edu

Andrew S. Petit — Department of Chemistry and Biochemistry, California State University—Fullerton, Fullerton, California 92834-6866, United States; Oorcid.org/0000-0002-9428-3499; Email: apetit@fullerton.edu

Authors

Ruby W. Neisser – Department of Chemistry, The College of William & Mary, Williamsburg, Virginia 23187-8795, United States

John P. Davis – Department of Chemistry, The College of William & Mary, Williamsburg, Virginia 23187-8795, United States

Megan E. Alfieri – Department of Chemistry, The College of William & Mary, Williamsburg, Virginia 23187-8795, United States

Hayden Harkins – Department of Chemistry and Biochemistry, California State University—Fullerton, Fullerton, California 92834-6866, United States

Complete contact information is available at: https://pubs.acs.org/10.1021/acs.jpca.3c04472

Notes

The authors declare no competing financial interest.

ACKNOWLEDGMENTS

This material is based upon work supported by the National Science Foundation to N.M.K. under Grant No. CHE-2102501. Partial support of this research from the Commonwealth Center for Energy and the Environment is also gratefully acknowledged by R.W.N., J.P.D., M.E.A., and N.M.K. N.M.K. also acknowledges William & Mary Research Computing for providing computational resources that contributed to the results reported within this paper. D.P.T. acknowledges support from the Robert A. Welch Foundation (Grant No. A-2049-20200401). Portions of this research were conducted with high-performance research computing resources provided by Texas A&M University HPRC. A.S.P. and H.H. acknowledge computational resources provided by the Center for Computational and Applied Mathematics at California State University, Fullerton.

REFERENCES

(1) Pachauri, R. K.; Allen, M. R.; Barros, V. R.; et al. Climate Change 2014: Synthesis Report. Contribution of Working Groups I, II and III to the Fifth Assessment Report of the Intergovernmental Panel on Climate Change; Pachauri, R. K., Meyer, L. A., Eds.; IPCC: Geneva, Switzerland, 2014; p 151.

(2) Lary, D. J.; Lee, A. M.; Toumi, R.; Newchurch, M. J.; Pirre, M.; Renard, J. B. Carbon Aerosols and Atmospheric Photochemistry. *J. Geophys. Res. Atmospheres* **1997**, *102*, 3671–3682.

- (3) Chung, S. H.; Seinfeld, J. H. Global Distribution and Climate Forcing of Carbonaceous Aerosols. *J. Geophys. Res. Atmospheres* **2002**, 107, 1–33.
- (4) Andreae, M. O.; Gelencsér, A. Black Carbon or Brown Carbon? The Nature of Light-Absorbing Carbonaceous Aerosols. *Atmospheric Chem. Phys.* **2006**, *6*, 3131–3148.
- (5) Laskin, A.; Laskin, J.; Nizkorodov, S. A. Chemistry of Atmospheric Brown Carbon. *Chem. Rev.* **2015**, *115*, 4335–4382.
- (6) Galloway, M. M.; Huisman, A. J.; Yee, L. D.; Chan, A. W. H.; Loza, C. L.; Seinfeld, J. H.; Keutsch, F. N. Yields of Oxidized Volatile Organic Compounds during the OH Radical Initiated Oxidation of Isoprene, Methyl Vinyl Ketone, and Methacrolein under High-NO_x Conditions. *Atmospheric Chem. Phys.* **2011**, *11*, 10779–10790.
- (7) Kusaka, R.; Nihonyanagi, S.; Tahara, T. The Photochemical Reaction of Phenol Becomes Ultrafast at the Air–Water Interface. *Nat. Chem.* **2021**, *13* (4), 306–311.

- (8) Finlayson-Pitts, B. J. Reactions at Surfaces in the Atmosphere: Integration of Experiments and Theory as Necessary (but Not Necessarily Sufficient) for Predicting the Physical Chemistry of Aerosols. *Phys. Chem. Chem. Phys.* **2009**, *11*, 7760–7779.
- (9) Lee, J. K.; Samanta, D.; Nam, H. G.; Zare, R. N. Micrometer-Sized Water Droplets Induce Spontaneous Reduction. *J. Am. Chem. Soc.* **2019**, *141*, 10585–10589.
- (10) Dobson, C. M.; Ellison, G. B.; Tuck, A. F.; Vaida, V. Atmospheric Aerosols as Prebiotic Chemical Reactors. *Proc. Natl. Acad. Sci. U. S. A.* **2000**, *97*, 11864–11868.
- (11) Ruiz-Lopez, M. F.; Francisco, J. S.; Martins-Costa, M. T. C.; Anglada, J. M. Molecular Reactions at Aqueous Interfaces. *Nat. Rev. Chem.* **2020**, *4*, 459–475.
- (12) Sobolewski, A. L.; Domcke, W. Photoejection of Electrons from Pyrrole into an Aqueous Environment: *Ab Initio* Results on Pyrrole-Water Clusters. *Chem. Phys. Lett.* **2000**, 321, 479–484.
- (13) Ishiyama, T.; Tahara, T.; Morita, A. Why the Photochemical Reaction of Phenol Becomes Ultrafast at the Air–Water Interface: The Effect of Surface Hydration. *J. Am. Chem. Soc.* **2022**, *144*, 6321–6325
- (14) Matsuzaki, K.; Kusaka, R.; Nihonyanagi, S.; Yamaguchi, S.; Nagata, T.; Tahara, T. Partially Hydrated Electrons at the Air/Water Interface Observed by UV-Excited Time-Resolved Heterodyne-Detected Vibrational Sum Frequency Generation Spectroscopy. *J. Am. Chem. Soc.* **2016**, *138*, 7551–7557.
- (15) Peterson, B. N.; Alfieri, M. E.; Hood, D. J.; Hettwer, C. D.; Costantino, D. V.; Tabor, D. P.; Kidwell, N. M. Solvent-Mediated Charge Transfer Dynamics of a Model Brown Carbon Aerosol Chromophore: Photophysics of 1-Phenylpyrrole Induced by Water Solvation. J. Phys. Chem. A 2022, 126, 4313–4325.
- (16) Kidwell, N. M. Photochemical and Photophysical Outcomes of Brown Carbon Chromophores: Insights from Laser Spectroscopy and Dynamics of Isolated Molecules and Complexes. In *Physical Chemistry Research at Undergraduate Institutions: Innovative and Impactful Approaches, Vol.* 2; ACS Symposium Series; American Chemical Society: 2022; Vol. 1429, pp 31–48.
- (17) Zhang, J.; Dolg, M. ABCluster: The Artificial Bee Colony Algorithm for Cluster Global Optimization. *Phys. Chem. Chem. Phys.* **2015**, *17*, 24173–24181.
- (18) Frisch, M. J.; Trucks, G. W.; Schlegel, G. W.; Scuseria, G. E.; Robb, M. A.; Cheeseman, J. R.; Scalmani, G.; Barone, V.; Petersson, G. A.; Nakatsuji, H.; et al. *Gaussian 16, Revision C.01*.
- (19) Rohrdanz, M. A.; Martins, K. M.; Herbert, J. M. A Long-Range-Corrected Density Functional That Performs Well for Both Ground-State Properties and Time-Dependent Density Functional Theory Excitation Energies, Including Charge-Transfer Excited States. *J. Chem. Phys.* **2009**, *130*, No. 054112.
- (20) Krylov, A. I. Equation-of-Motion Coupled-Cluster Methods for Open-Shell and Electronically Excited Species: The Hitchhiker's Guide to Fock Space. *Annu. Rev. Phys. Chem.* **2008**, *59*, 433–462.
- (21) Jacquemin, D.; Duchemin, I.; Blase, X. 0–0 Energies Using Hybrid Schemes: Benchmarks of TD-DFT, CIS(D), ADC(2), CC2, and BSE/GW Formalisms for 80 Real-Life Compounds. J. Chem. Theory Comput. 2015, 11, 5340–5359.
- (22) Dempwolff, A. L.; Schneider, M.; Hodecker, M.; Dreuw, A. Efficient Implementation of the Non-Dyson Third-Order Algebraic Diagrammatic Construction Approximation for the Electron Propagator for Closed- and Open-Shell Molecules. *J. Chem. Phys.* **2019**, *150*, No. 064108.
- (23) Loos, P.-F.; Jacquemin, D. Is ADC(3) as Accurate as CC3 for Valence and Rydberg Transition Energies? *J. Phys. Chem. Lett.* **2020**, 11, 974–980.
- (24) Plasser, F.; Wormit, M.; Dreuw, A. New Tools for the Systematic Analysis and Visualization of Electronic Excitations. I. Formalism. *J. Chem. Phys.* **2014**, *141*, No. 024106.
- (25) Martin, R. L. Natural Transition Orbitals. J. Chem. Phys. 2003, 118, 4775-4777.
- (26) Epifanovsky, E.; Gilbert, A. T. B.; Feng, X.; Lee, J.; Mao, Y.; Mardirossian, N.; Pokhilko, P.; White, A. F.; Coons, M. P.;

- Dempwolff, A. L.; et al. Software for the Frontiers of Quantum Chemistry: An Overview of Developments in the Q-Chem 5 Package. *J. Chem. Phys.* **2021**, *155*, No. 084801.
- (27) Colbert, D. T.; Miller, W. H. A Novel Discrete Variable Representation for Quantum Mechanical Reactive Scattering via the S-matrix Kohn Method. *J. Chem. Phys.* **1992**, *96*, 1982.
- (28) Pitzer, K. S. Energy Levels and Thermodynamic Functions for Molecules with Internal Rotation: II. Unsymmetrical Tops Attached to a Rigid Frame. *J. Chem. Phys.* **1946**, *14*, 239–243.
- (29) Korn, J. A.; Tabor, D. P.; Sibert, E. L.; Zwier, T. S. Conformation-Specific Spectroscopy of Alkyl Benzyl Radicals: Effects of a Radical Center on the CH Stretch Infrared Spectrum of an Alkyl Chain. *J. Chem. Phys.* **2016**, *145* (12), 124314.
- (30) Sibert, E., III Modeling Vibrational Anharmonicity in Infrared Spectra of High Frequency Vibrations of Polyatomic Molecules. *J. Chem. Phys.* **2019**, *150*, No. 090901.
- (31) The S_1 relative energy at $\phi_{\rm symm}=90^\circ$ is approximated from a cubic spline through calculated electronic structure data. Despite repeated attempts, we were unable to obtain an optimized geometry at $\phi_{\rm symm}=90^\circ$ on S_1 .
- (32) Hockridge, M. R.; Robertson, E. G.; Simons, J. P.; Borst, D. R.; Korter, T. M.; Pratt, D. W. The $S_1 \leftarrow S_0$ Electronic Transitions of 4-and 5-Phenyl Imidazole in the Gas Phase. *Chem. Phys. Lett.* **2001**, 334, 31–38.
- (33) Robertson, E. G.; Thompson, C. D.; Morrison, R. J. S. Interplanar Torsion in the $S_1 \leftarrow S_0$ Electronic Spectrum of Jet Cooled 1-Phenylimidazole. *J. Chem. Phys.* **2004**, *121*, 12421–12427.
- (34) Contreras-García, J.; Johnson, E. R.; Keinan, S.; Chaudret, R.; Piquemal, J.-P.; Beratan, D. N.; Yang, W. NCIPLOT: A Program for Plotting Noncovalent Interaction Regions. *J. Chem. Theory Comput.* **2011**, *7*, 625–632.
- (35) van den Brom, A. J.; Kapelios, M.; Kitsopoulos, T. N.; Nahler, N. H.; Cronin, B.; Ashfold, M. N. R. Photodissociation and Photoionization of Pyrrole Following the Multiphoton Excitation at 243 and 364.7 nm. *Phys. Chem. Chem. Phys.* **2005**, *7*, 892–899.
- (36) Lippert, H.; Ritze, H.-H.; Hertel, I. V.; Radloff, W. Femtosecond Time-Resolved Hydrogen-Atom Elimination from Photoexcited Pyrrole Molecules. *ChemPhysChem* **2004**, *5*, 1423–1427
- (37) Kumar, A.; Kołaski, M.; Kim, K. S. Ground State Structures and Excited State Dynamics of Pyrrole-Water Complexes: *Ab Initio* Excited State Molecular Dynamics Simulations. *J. Chem. Phys.* **2008**, 128, No. 034304.
- (38) Neville, S. P.; Mirmiran, A.; Worth, G. A.; Schuurman, M. S. Electron transfer in photoexcited pyrrole dimers. *J. Chem. Phys.* **2019**, *151*, 164304.
- (39) Neville, S. P.; Kirkby, O. M.; Kaltsoyannis, N.; Worth, G. A.; Fielding, H. H. Identification of a New Electron-Transfer Relaxation Pathway in Photoexcited Pyrrole Dimers. *Nat. Commun.* **2016**, *7*, 11357.
- (40) Montero, R.; León, I.; Fernández, J. A.; Longarte, A. Femtosecond Excited State Dynamics of Size Selected Neutral Molecular Clusters. J. Phys. Chem. Lett. 2016, 7, 2797–2802.
- (41) Tabor, D. P.; Kusaka, R.; Walsh, P. S.; Sibert, E. L. I.; Zwier, T. S. Isomer-Specific Spectroscopy of Benzene–(H₂O)n, n = 6,7: Benzene's Role in Reshaping Water's Three-Dimensional Networks. *J. Phys. Chem. Lett.* **2015**, *6*, 1989–1995.
- (42) Wu, B.; Xie, F.; Xu, Y. The Pyrrole-Water Complex: Multidimensional Large Amplitude Dynamics and Rotational Spectra of Its ¹³C Isotopologues. *J. Mol. Spectrosc.* **2020**, *374*, 111381.
- (43) Matsumoto, Y.; Honma, K. Hydrogen-bonded structures of pyrrole-solvent clusters: Infrared cavity ringdown spectroscopy and quantum chemical calculations. *J. Chem. Phys.* **2009**, *130*, No. 054311. (44) Sarkar, S.; Ramanathan, N.; Sundararajan, K. Effect of Methyl
- (44) Sarkar, S.; Ramanathan, N.; Sundararajan, K. Effect of Methyl Substitution on the N–H···O Interaction in Complexes of Pyrrole with Water, Methanol, and Dimethyl Ether: Matrix Isolation Infrared Spectroscopy and *Ab Initio* Computational Studies. *J. Phys. Chem. A* **2018**, 122, 2445–2460.

(45) Carney, J. R.; Zwier, T. S. Infrared and Ultraviolet Spectroscopy of Water-Containing Clusters of Indole, 1-Methylindole, and 3-Methylindole. *J. Phys. Chem. A* **1999**, *103*, 9943–9957.